



Evolution of turbulence using a random jet array

Arefe Ghazi Nezami ^{*} and Blair Anne Johnson [†]*Fariborz Maseeh Department of Civil, Architectural and Environmental Engineering,
The University of Texas at Austin, Austin, Texas 78712, USA*

(Received 6 November 2023; accepted 22 May 2024; published 26 July 2024)

Random jet arrays (RJAs) have been shown to be effective in generating zero mean flow homogeneous isotropic turbulence. While many laboratory studies have investigated the flow in these facilities, there are several remaining questions regarding the evolution of turbulence, from the development of turbulence to where it decays, along with understanding how input energy from the jet array transfers into different turbulent flow characteristics. To address these questions, we perform a series of laboratory experiments in which we alter the parameters of the randomized algorithm, along with the jet spacing and outlet velocity of the jets. We first determine the location where turbulence transitions to a fully developed state and show that it is a function of jet penetration length, \mathcal{L}_J , and effective jet spacing, S_e . We identify three distinct regions for the spatial decay of turbulence in RJA facilities and notably, we find different decay rates, unlike previous studies that report only one spatial decay rate using similar facilities. These regions are shown to depend on the variations of input parameters yet independent of the strength of the mean flow. We also find the strength of the mean flow does not affect the homogeneity, nor the production, transport, or advection terms of the turbulent kinetic energy budget equation. Finally, we address a longstanding question toward estimating turbulence metrics with an RJA based on the input parameters. We define an efficiency parameter that provides insight into the transfer rate of input power to the dissipation rate of the generated turbulence.

DOI: [10.1103/PhysRevFluids.9.074610](https://doi.org/10.1103/PhysRevFluids.9.074610)

I. INTRODUCTION

Generating homogeneous isotropic turbulence (HIT) in the laboratory has been of great interest for several decades. HIT absent any mean flow or mean shear is useful to study fundamental aspects of flow energetics to explore boundary layer dynamics [1,2], mass transfer and mixing across interfaces [3], mobility of inertial particles [4], ice melting [5], and many other topics. In laboratory settings, zero-mean-shear turbulence has been developed in water flumes and wind tunnels with moving beds [6–8], while low-mean-flow turbulence can be generated in tanks using devices such as oscillating grids (see, e.g., Refs. [9,10]), jets (e.g., Ref. [11]), rotating plates (e.g., Refs. [12]), loudspeakers (e.g., Ref. [13]), and fans (e.g., Ref. [14]). Within these facilities, there typically exists a limited region where the flow is both statistically homogeneous and isotropic, depending on the type of forcing and configuration of the experimental facility [15].

In setups that generate low-mean-flow turbulence, synthetic jets are commonly used to drive flows. Synthetic jets, as defined by Glezer and Amitay [16], use the working fluid within the system to induce momentum without net mass flux. In this context, many actuators such as fans, loudspeakers, rotating elements, and jets, can be considered synthetic jets [15]. These actuators

*Contact author: aghazinezami@utexas.edu

†Contact author: blairjohnson@utexas.edu

are typically designed to introduce randomness through factors such as the duration of rotational direction, or on-and-off periods in the forcing. This randomness leads to different flow patterns compared with conventional synthetic jets [16]. In this study, we refer to jets as synthetic jets in the sense that they only induce momentum, whereas the synthetic jets reviewed in Glezer and Amitay [16] are referred to as conventional pulsating synthetic jets.

While not all turbulence-generating mechanisms have been shown to create HIT with truly zero mean flow, random jet arrays (RJAs) have been shown to generate HIT with substantial turbulent kinetic energy (TKE) and negligible recirculation [1,17]. In RJAs, synthetic jets are individually actuated to input the required momentum to generate turbulence. Synthetic jets can be arranged in one or multiple arrays, or deployed individually in facilities, to create customized flow environments to study applications such as sediment transport [18], effects of background flows on jets [19,20], electrodeposition [21], and dissolution of particles [22].

To generate high values of turbulent kinetic energy and low values of mean flow, RJAs typically use the “sunbathing” algorithm [1,23]. This algorithm prescribes the mean on- and off-times of each jet (T_{on} and T_{off} , respectively), using Gaussian distributions to randomize jet actuation about these mean times. When using a planar RJA, the flow structure in the tank is divided into distinct regions. Immediately adjacent to the array is a jet-dominated region, where instantaneous jet activity drives strong flows away from and towards the jet-orifice plane. This is followed by a merging region, where the jets interact with one another to form HIT. Beyond this is the mixed region: the individual jets have sufficiently been stirred into the ambient, turbulence is fully developed and the decay of turbulent kinetic energy starts. Finally, in the presence of an interface opposite from a single planar RJA, there may be a boundary-influenced flow region where a wall, free-surface, or other type of interface influences the flow, causing the isotropy to break down [2]. By contrast, in setups where multiple RJAs face each other (see, e.g., Refs. [24,25]), the turbulent flows generated by each RJA interact with each other to maintain an isotropic region centered within the facility.

Several mechanisms for generating turbulent flow with RJAs have been investigated in recent years, considering variables such as T_{on} , φ_{on} (mean percentage of active jets at a given time), U_J (jet outlet velocity), proximity of the RJA to a boundary, and others. Johnson and Cowen [2] investigated the effect of T_{on} on turbulence statistics, specifically finding higher values of turbulent kinetic energy, dissipation rates, and integral length scale with increasing T_{on} . Both Johnson and Cowen [2] and Variano and Cowen [1] found the turbulent generation to be relatively independent of φ_{on} over a specified range of φ_{on} . Pérez-Alvarado *et al.* [23] explored the importance of spatial correlations in the driving algorithm across the jet array; they found that when using the random algorithm (i.e., with no defined spatial correlation between active pumps), high turbulent kinetic energy with the lowest mean flow was achieved. Carter *et al.* [25] varied jet spacing, S , in the array and found no relation between the integral length scale and S , instead suggesting that the integral length scale depends on the characteristics of the jets themselves. In a recent review, Ghazi Nezami *et al.* [15] synthesized the underlying influence of geometric dimensions of turbulence-generating facilities on the resultant turbulence properties. They identified a new length scale of RJAs that is a counterpart to the geometric jet spacing, termed the *effective jet spacing*, S_e , which is strongly correlated with several turbulence metrics. They defined S_e based on the jet spacing in a hypothetical equivalent array of jets that has a total number of average active jets (e.g., $N\varphi_{\text{on}}$, where N is the total number of jets within the array) evenly spaced across the same area as the original array of jets. Thus, whereas S describes the proximity of jets that will be active at some time during the duration of testing, S_e provides an average measure of the distance between *active* jets at any instant.

Several key aspects of random jet arrays and the associated forcing algorithms remain insufficiently explored, prompting the need for further investigation. The spatial evolution of flow characteristics within an RJA facility has been a relatively understudied aspect of existing research. Many studies declare to achieve negligible mean flow. However, the specific conditions required to achieve this state within an RJA facility, and the influence of mean flows on turbulence statistics in cases where mean flows are present, remain unknown. Furthermore, a significant knowledge gap persists regarding the correlation between the input energy supplied to the system through actuators

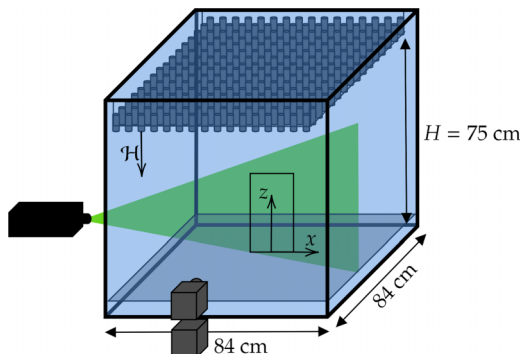


FIG. 1. Schematic of the experimental setup, showing laser light sheet, two-camera setup for PIV, and FOV with coordinate system.

(e.g., pumps) and the resultant energy of the turbulence. In this study, we aim to address these gaps by examining the impact of RJA input parameters on the spatially evolving characteristics of turbulence. To accomplish this, a series of experiments is performed with two distinct jet spacings in a planar RJA submerged in a water tank. For each S , the inputs of the sunbathing algorithm (i.e., T_{on} , φ_{on}) and the outlet velocities of the jets, U_J , are all systematically varied to investigate the flow energetics.

The paper is structured as follows: in Sec. II the apparatus and measurement techniques are described. In Sec. III, the evolution, decay, and characteristics of the turbulence are investigated. In Sec. IV, the connection between the input energy and the resultant turbulent flow is elucidated. Lastly, in Sec. V a summary of the findings of this study is presented.

II. EXPERIMENTAL SETUP

A. Apparatus

Experiments were conducted in a water tank at the Johnson Environmental Turbulence Laboratory (JETLab) of the Center for Water and the Environment (CWE) at The University of Texas at Austin. The tank has a height of 100 cm with a cross-sectional area of $84 \times 84 \text{ cm}^2$, as depicted in Fig. 1. The random-jet array is suspended at the top of the tank, spanning the cross-sectional area and fully submerged. An acrylic plate is placed at the bottom of the tank to provide a rigid, no-slip boundary. In all experiments performed herein, the distance between the orifice plane of the jet array and the bottom boundary is 75 cm. The coordinate system is shown in Fig. 1, with $(x, y, z) = (0, 0, 0)$ located at the center of the bottom boundary, and the z coordinate increasing upwards. U , V , and W are the velocities in the x , y , and z directions, respectively. Due to the distributed forcing across the x - y plane, we assume radial symmetry of the flow in the horizontal direction (e.g., U and V are expected to be statistically equivalent), as in Johnson and Cowen [2].

Rule il200 submersible inline pumps with operation specifications of 12 V, 2.8 A are used in the RJA. Each pump intakes water from above and expels water downward through the bottom orifice with an outlet diameter d_j of 8 mm. These pumps have a stated maximum outlet flow rate of 200 GPH when operated at 12 V. We define a nominal jet Reynolds number, $\text{Re}_j \equiv U_j d_j / \nu$, with ν being the kinematic viscosity of water at 20 °C. For the studies performed herein, U_j was varied from 3.0 to 4.2 m/s by altering the supplied voltages, and Re_j varied from 22 800 to 31 900, respectively. Two different array configurations were used— 8×8 and 16×16 . The 8×8 array was achieved by selectively operating jets in the 16×16 RJA. The distance between the centers of the pump outlets in the 16×16 and 8×8 array setups are $S = 5$ and 10 cm, respectively.

The on-off states of the pumps are determined via the sunbathing algorithm, [1]. Each jet-operation state is selected from a Gaussian distribution with a given T_{on} and standard deviation,

σ_{on} , where $\sigma_{\text{on}} = \frac{1}{3}T_{\text{on}}$ [1]. The input variable φ_{on} determines the mean percentage of jets that are operating at a given time. T_{off} is determined by $\varphi_{\text{on}} = T_{\text{on}}/(T_{\text{on}} + T_{\text{off}})$. As in Johnson and Cowen [2], a matrix of pump-operation states is generated using MATLAB. The operation matrix is read by a 16 MHz Arduino Mega 2560 microcontroller at an update frequency of 10 Hz. The Arduino controls the operational settings of the pumps using a 32-byte data transfer. Each byte contains information for eight jets. This information is then sent to shift registers (Texas Instrument SN74HC595N) and integrated MIC2981/82YN circuit driver arrays on the pump control boards, produced by PJC Solutions. The pumps are driven by an AMETEK Sorensen SGA series programmable power supply (Model SGA15X267E), which has a maximum power output of 15 kW and a current capacity of 267 A. A total of 39 different experiments were performed with systematic combinations of input variables to investigate the formation and decay of turbulence. Each experiment lasted 25 minutes to ensure statistical convergence of flow metrics [1].

B. Measurement technique

Particle image velocimetry (PIV) [26] is used to collect velocity data nonintrusively. A 10 W 532 nm Opto Engine Diode-Pumped Solid-State (DPSS) laser illuminates the x - z plane at the lateral center of the tank. The water is seeded with ORGASOL (R) 2002 ES 3 Nat 3 Polyamide 12 nylon particles from Arkema Group, with a specific gravity, S_g , of 1.03. The particles have a batch-average diameter, D_b , of 29.4 μm , with 8% greater than 40 μm and 5% less than 20 μm . The Stokes number is calculated as the ratio of the relaxation timescale (τ_R) to the Kolmogorov timescale (τ_η , discussed below) where the relaxation timescale is computed as $\tau_R = S_g D_b^2 / 18\nu$. For these particles, $St < 0.01$, indicating the particles passively follow the flow for accurate data collection.

Two Imperx CMOS 12 MP charged-coupled device (CCD) cameras (Model PIV01882 from TSI Inc.), equipped with a 3000 \times 4000 pixel sensor are used for capturing PIV images. The pixel values are digitized at 10 bits per pixel. One camera is positioned to capture images at the bottom boundary with a field of view (FOV) 19 cm wide and 19 cm tall. For some experiments in which a taller measurement region is desired, the two cameras are mounted atop one another (with 2 cm of overlap). The second camera covers an area of 19 cm wide and 24 cm tall, extending the overall height of the FOV to a total of 43 cm. The cameras and the laser are triggered through a TSI LaserPulse Synchronizer (Model 610036), and the timing of laser pulses and camera shutters are controlled through TSI Insight 4G software. Image pairs are captured at a sampling frequency of 1 Hz with a separation time Δt within pairs ranging from 4 to 6 ms, depending on the flow parameters.

To enhance contrast of the tracer particles, the images are preprocessed. Background images are constructed by estimating the minimum light intensity recorded at each pixel for the first and second images within each pair. These background images are subtracted from each PIV image. The velocity field at each time step is then calculated using PIVlab [27]. For PIV processing, each image is divided into 80 \times 80 pixel interrogation windows (IW) with a 50% overlap for the first interrogation, followed by two passes with 40 \times 40 pixel IWs, also at 50% overlap. Velocity vectors are calculated for each IW with an area of 0.065 cm², and a vector spacing of 0.13 cm. PIVlab utilizes Fast Fourier Transform (FFT) and cross-correlation techniques to determine particle displacements within each IW. To eliminate outliers caused by global image artifacts, an adaptive Gaussian filter is applied to the calculated velocity vectors at each time step [28]. This filter adjusts its smoothing radius according to the local velocity gradient, effectively eliminating outliers while preserving fine-scale turbulent velocity structures. Subsequently, a spatial median filter is applied at the local scale using a user-defined threshold to remove erroneous vectors [2,29].

The PIV data in this study provide velocity fields U and W in the x - z plane, where $\mathbf{U} = (U, W)$. Throughout our analysis, spatial averaging of parameters is denoted by an overbar, and temporal averaging is shown by angle brackets. The fluctuating velocities, $\mathbf{u} = (u, w)$ are calculated by subtracting the time-averaged velocities from the instantaneous velocities, $\mathbf{u} = \mathbf{U} - \langle \mathbf{U} \rangle$ at each location in the FOV. The root mean square (RMS) of the fluctuating velocities $\mathbf{u}' = (u', w')$ are

computed as $u'_i = (\langle u_i^2 \rangle)^{1/2}$. Uncertainty bounds of flow statistics are calculated with the bootstrap technique [30]. To achieve a 95% confidence interval (CI), the 97.5% and 2.5% percentile statistics are used.

III. EVOLUTION OF TURBULENCE IN THE random jet array FACILITY

A. The onset of turbulence

The generation of turbulence using an RJA starts with injections of momentum from synthetic jets, resulting in local velocity gradients from interactions of adjacent jets and the ambient flow. Given an RJA with downward-facing pumps, the region immediately downstream of the RJA orifice plane (i.e., the jet-merging region), exhibits a high downward mean velocity (with local upward return flows) and significant anisotropy due to the input momentum from individual pump activity. In this region, the jets interact with each other, triggering energy transfer from the axially dominant mean jet flows into turbulent kinetic energy.

While a jet-merging region exists for all planar jet arrays, we observe disparities in its characteristics when comparing different RJA input parameters. To highlight different features of the jet-merging region, we first compare the time-averaged contour maps of the flow characteristics of select representative cases. Figure 2 illustrates the difference in the mean horizontal and vertical velocities, turbulent kinetic energy [i.e., $k = \frac{1}{2}(2u'^2 + w'^2)$ assuming radial symmetry], mean-flow strength (i.e., M^* , the ratio of the mean kinetic energy to the turbulent kinetic energy as introduced by Variano and Cowen [1]), and isotropy ratio (i.e., $\Omega = u'/w'$), in the measurement region. The tests in Fig. 2 are selected to provide comparison between cases with different T_{on} [i.e., Figs. 2(a) and 2(b)], U_J [i.e., Figs. 2(b) and 2(c)], ϕ_{on} [i.e., Figs. 2(b) and 2(d)], and the interjet spacing, S [i.e., Figs. 2(c) and 2(e)].

Comparing Figs. 2(a), 2(b), and 2(c) reveals that increasing T_{on} , U_J , and ϕ_{on} results in higher downward velocity at the top of the FOV. Furthermore, increasing these variables results in higher magnitudes of k over a prolonged region. Importantly, when comparing the contour map of \bar{W} close to the RJA with the 8×8 RJA [see upper-right region of \bar{W} in Fig. 2(e)] to the 16×16 RJA [see Fig. 2(c)], we observe that the activity of an individual jet is more pronounced in the less dense array due to the increased likelihood of unmerged jets—see top of Fig. 2(d).

In all cases, there exist return flows and toroidal mean circulations to balance out the axial flow of the pumps. Variano and Cowen [1] defined mean flows to be negligible below a threshold of M^* equal to 5%. Figures 2(a) and 2(b) demonstrate that the magnitude of M^* for $T_{\text{on}} = 0.2$ s is notably higher compared with $T_{\text{on}} = 0.8$ s. In the case of $T_{\text{on}} = 0.2$ s, there are regions where the mean kinetic energy and turbulent kinetic energy are equal [i.e., M^* is of $O(1)$]; this effect is enhanced at higher ϕ_{on} (see Tables I and II). Since the magnitude of M^* exceeds this threshold in certain cases within our setup, it becomes crucial to ascertain whether mean recirculations introduce high spatial velocity gradients or affect homogeneity. This subject will be discussed in Sec. III B. The isotropy ratio has consistent values among different cases and throughout the FOV, with the exception of near the bottom boundary.

As is apparent in the upper region of Fig. 2, k increases with distance from the RJA in the jet-merging region. This is also shown in Fig. 3, where k increases up to a certain distance from the RJA and subsequently decreases. When k reaches its maximum value k_{max} , the turbulence is fully developed and the jet merging region has ended. This does not mean that turbulence generation ceases beyond this point, rather it means that production from jet flows is not the dominant mechanism.

The location of k_{max} varies among different cases (see Fig. 3). We define \mathcal{H}_{max} as the distance from the jet array to the location of k_{max} , recalling the jet orifice plane is positioned at $z = 72$ cm. We refer to the region beyond \mathcal{H}_{max} as the developed turbulent region. In each panel of Fig. 3, only one of the input variables is modified to illustrate the influence of that parameter on \mathcal{H}_{max} . According to Figs. 3(a) and 3(b), both RJAs exhibit an increase in k_{max} and \mathcal{H}_{max} with increasing T_{on} . Using

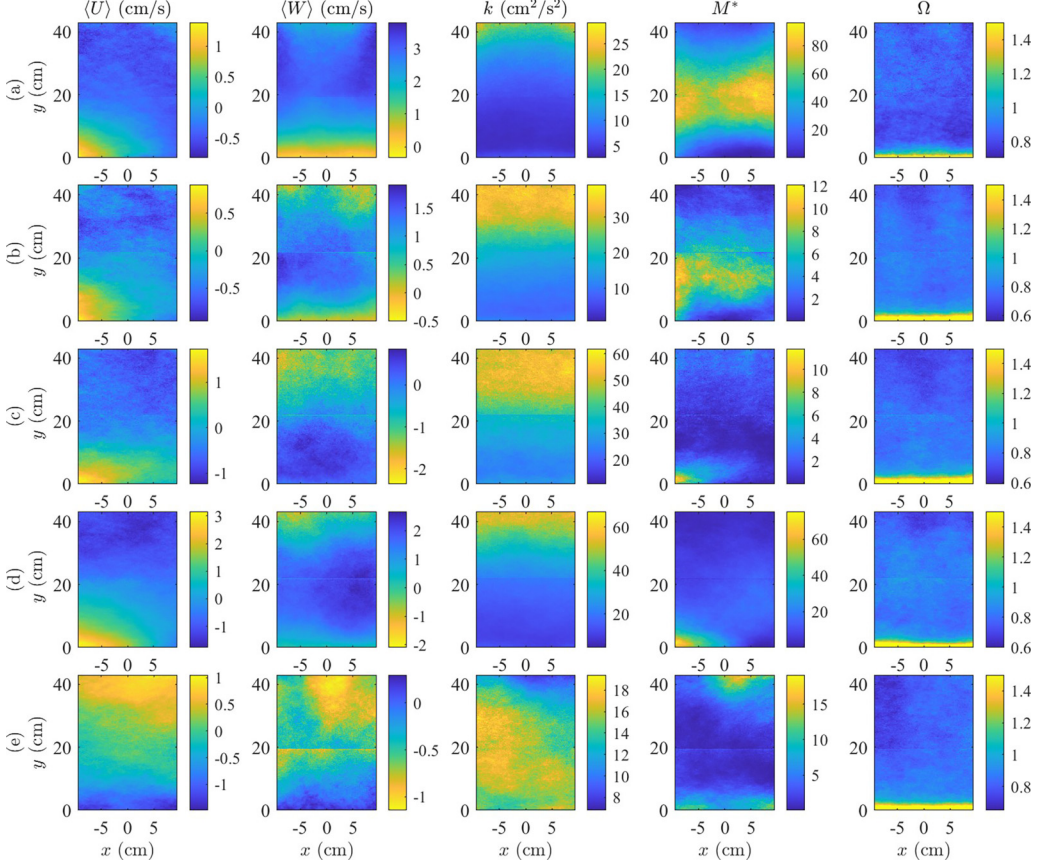


FIG. 2. Contour map of temporally-averaged velocities, turbulent kinetic energy, mean flow strength, and isotropy ratio for (a) 16×16 RJA for $T_{\text{on}} = 0.2$ s, $\varphi_{\text{on}} = 5\%$, and $U_J = 3.0$ m/s, (b) 16×16 RJA for $T_{\text{on}} = 0.8$ s, $\varphi_{\text{on}} = 5\%$, and $U_J = 3.0$ m/s, (c) 16×16 RJA for $T_{\text{on}} = 0.8$ s, $\varphi_{\text{on}} = 5\%$, and $U_J = 4.2$ m/s, (d) 16×16 RJA for $T_{\text{on}} = 0.8$ s, $\varphi_{\text{on}} = 10\%$, and $U_J = 3.0$ m/s, (e) 8×8 RJA for $T_{\text{on}} = 0.8$ s, $\varphi_{\text{on}} = 5\%$, and $U_J = 4.2$ m/s.

the same T_{on} with a denser array (i.e., lower S) results in reaching the fully developed state of turbulence at a shorter distance (i.e., smaller \mathcal{H}_{max}). For example, in Fig. 3(b) for $T_{\text{on}} = 0.2$ s, \mathcal{H}_{max} must be located above the FOV, whereas in Fig. 3(a) for the same T_{on} , \mathcal{H}_{max} is located within the FOV. Figure 3(c) demonstrates that increasing U_J increases \mathcal{H}_{max} , due to an increase in momentum imposed by the active jets. Figure 3(d) shows that increasing φ_{on} results in a decrease to \mathcal{H}_{max} . This can be explained by considering the variable S_e , introduced by Ghazi Nezami *et al.* [15]. According to Ghazi Nezami *et al.* [15], S_e represents the distance between the average number of operating jets (i.e., $N\varphi_{\text{on}}$), when distributed evenly across the array. Increasing φ_{on} , which concurrently decreases S_e , results in a decrease to \mathcal{H}_{max} , due to increased likelihood of jet interactions.

To characterize the dependence of \mathcal{H}_{max} on the RJA inputs, we define a parameter, $\mathcal{L}_{\mathcal{J}}$, which indicates a characteristic depth of influence for an individual jet and provides a means of comparing the strength of jet flows based on the time of operation and outlet velocity. Parameter $\mathcal{L}_{\mathcal{J}}$ relies upon the centerline jet velocity U_c , which decays with distance from the jet orifice plane (i.e., $\mathcal{H} = H - z$). The evolution of U_c of a single jet follows $U_c(\mathcal{H})/U_J = Bd_J/(\mathcal{H} - \mathcal{H}_0)$, where B is an empirical constant and \mathcal{H}_0 represents the virtual origin of the jet [31]. By taking $\mathcal{L}_{\mathcal{J}} = U_c T_{\text{on}}$ and $\mathcal{L}_{\mathcal{J}} = \mathcal{H} - \mathcal{H}_0$, and replacing these in the previous equation, we get an approximate penetration

TABLE I. Turbulence statistics across all input parameters for 8×8 RJA. 95% confidence intervals shown in brackets.

T_{on} (s)	φ_{on} (%)	U_J (cm/s)	u' (cm/s)	w' (cm/s)	\bar{U} (cm/s)	\bar{W} (cm/s)	k (cm ² /s ²)	Ω	$\Omega_{\mathcal{L}}$	M^* (%)	\mathcal{L}_L (cm)	ϵ (cm ² /s ³)	η (cm)	λ_g λ_g (cm)	Re_λ	
0.2	5	4.2	1.45	1.54	-1.06	1.468	3.29	0.94	2.05	51.7	3.91	0.9	0.0324	0.603	89	
			[1.44,1.46]	[1.53,1.55]	[-1.07,-1.06]	[1.41,1.52]	[3.27,3.34]									
0.4	5	4.2	2.12	2.28	-0.79	1.038	7.194	0.93	1.83	22.9	4.65	2.1	0.0263	0.585	128	
			[2.12,2.12]	[2.21,2.33]	[-0.82,-0.76]	[1.03,1.06]	[6.95,7.26]									
0.6	5	4.2	2.79	3.3	-0.43	0.596	13.5	0.85	1.47	5.0	4.69	3.78	0.0227	0.598	179	
			[2.78,2.80]	[3.29,3.32]	[-0.44,-0.42]	[0.55,0.64]	[13.47,13.55]									
	10	3.5	2.6	2.76	-0.22	1.038	10.71	0.94	2.02	18.2	4.73	3.16	0.0237	0.582	156	
			[2.60,2.61]	[2.72,2.82]	[-0.29,-0.20]	[0.88,1.20]	[10.67,10.84]									
15	4.2	3.5	3.15	3.41	-0.60	1.714	15.65	0.92	1.80	19.7	4.86	4.25	0.022	0.607	196	
			[3.14,3.15]	[3.35,3.45]	[-0.70,-0.54]	[1.40,1.83]	[15.59,15.68]									
0.8	5	3.5	2.55	2.94	-0.20	0.083	10.73	0.87	1.56	3.0	4.72	3.55	0.023	0.55	147	
			[2.52,2.56]	[2.93,2.95]	[-0.22,-0.19]	[-0.02,0.19]	[10.68,10.78]									
	10	4.2	3.5	3.07	3.62	-0.22	0.409	16.04	0.85	1.43	2.4	4.62	4.45	0.0218	0.6	196
				[3.07,3.08]	[3.60,3.65]	[-0.23,-0.22]	[0.40,0.43]	[15.94,16.14]								
15	4.2	3.5	2.82	3.05	-0.38	1.154	12.61	0.93	1.72	15.0	4.68	3.95	0.0224	0.565	164	
			[2.80,2.83]	[3.00,3.08]	[-0.473,-0.32]	[1.02,1.24]	[12.52,12.66]									
1.0	5	4.2	3.51	3.82	-0.19	1.12	19.57	0.92	1.64	11.2	5.13	5.79	0.0204	0.581	210	
			[3.47,3.53]	[3.80,3.85]	[-0.26,-0.12]	[0.90,1.37]	[19.54,19.64]									
	10	4.2	3.5	3.11	3.33	-0.79	1.099	15.1	0.93	1.85	16.8	4.63	4.6	0.0216	0.573	182
				[3.07,3.17]	[3.28,3.38]	[-0.85,-0.74]	[0.95,1.16]	[15.03,15.18]								
15	4.2	3.5	3.73	4.07	-0.64	1.173	22.03	0.92	1.88	12.5	4.69	6.39	0.0199	0.587	225	
			[3.73,3.75]	[4.00,4.11]	[-0.79,-0.51]	[1.05,1.27]	[21.93,22.19]									
1.0	5	4.2	3.24	4	0.16	0.54	18.34	0.81	1.15	8.8	5.17	5.05	0.0211	0.603	211	
			[3.23,3.24]	[3.78,4.29]	[0.11,0.18]	[0.25,0.90]	[17.60,19.90]									

depth as shown in Eq. (1):

$$\mathcal{L}_{\mathcal{J}} = \sqrt{d_J U_J T_{\text{on}}}. \quad (1)$$

We assume the outlet flow of individual pumps decays similarly to a single jet for $\mathcal{H} \leq \mathcal{L}_{\mathcal{J}}$. According to Pope [31], at a distance of $\mathcal{L}_{\mathcal{J}}$, the half-width of a jet is equal to $3C\mathcal{L}_{\mathcal{J}}$, where constant $C \propto 0.1$. A factor of 3 is included to ensure the velocity at the outer edge of the pump outlet flow goes to zero. When $3 \times 0.1\mathcal{L}_{\mathcal{J}} < S_e$, the jets do not interact. This relation holds even for our longest $\mathcal{L}_{\mathcal{J}}$ and smallest S_e . Therefore, assuming that each jet acts as an individual jet for approximating $\mathcal{L}_{\mathcal{J}}$ is valid.

To incorporate the effects of S and φ_{on} into a nondimensional parameter that encompasses all input variables of the RJA, we recall S_e and propose $\mathcal{L}_{\mathcal{J}}/S_e$ as the normalized jet penetration depth. Figure 4 reveals that \mathcal{H}_{max} (when nondimensionalized with S_e) is positively correlated with $\mathcal{L}_{\mathcal{J}}/S_e$, following a relationship $\mathcal{H}_{\text{max}}/S_e = 1.8(\mathcal{L}_{\mathcal{J}}/S_e)^{0.56}$. Increasing $\mathcal{L}_{\mathcal{J}}/S_e$, which is equivalent to decreasing U_J and T_{on} , in conjunction with increasing φ_{on} (i.e., decreasing S_e), results in k reaching its maximum value closer to the jet array (i.e., reducing \mathcal{H}_{max}), thus providing a larger region of developed turbulence. We find $\mathcal{H}_{\text{max}} < 2.5\mathcal{L}_{\mathcal{J}}$ in all of our experiments.

TABLE II. Turbulence statistics across all input parameters for 16×16 RJA. 95% confidence intervals shown in brackets.

T_{on} (s)	φ_{on} (%)	U_J (cm/s)	u' (cm/s)	w' (cm/s)	\bar{U} (cm/s)	\bar{W} (cm/s)	k (cm ² /s ²)	Ω	$\Omega_{\mathcal{L}}$	M^* (%)	\mathcal{L}_L (cm)	ϵ (cm ² /s ³)	η (cm)	λ_g (cm)	Re_λ
0.2	5	3.0	1.64	1.99	-0.15	-2.4	4.70	0.87	1.60	46.7	2.67	1.91	0.0269	0.496	88
			[1.63,1.64]	[1.98,2.01]	[-0.20,-0.11]	[-2.42,-2.39]	[4.67,4.77]								
	3.5	1.97	2.53	-0.18	-2.74	7.138	0.78	1.05	41.7	2.87	2.47	0.0252	0.538	117	
		[1.97,2.00]	[2.53,2.53]	[-0.26,-0.15]	[-2.79,-2.73]	[7.12,7.15]									
	4.2	2.33	2.8	-0.20	-3.14	9.392	0.83	1.32	45.6	3.71	4.33	0.0219	0.466	117	
		[2.32,2.33]	[2.80,2.81]	[-0.27,-0.13]	[-3.17,-3.12]	[9.37,9.43]									
10	3.0	2.38	2.83	0.19	-2.77	9.709	0.84	1.89	48.6	3.79	3.30	0.0235	0.542	138	
	[2.38,2.39]	[2.82,2.84]	[0.08,0.37]	[-2.78,-2.73]	[9.63,9.77]										
15	3.0	2.12	2.42	0.88	-2.25	7.544	0.88	1.77	57.6	4.62	2.29	0.0257	0.574	129	
	[2.12,2.13]	[2.40,2.44]	[0.76,0.97]	[-2.30,-2.20]	[7.40,7.62]										
0.4	5	3.0	1.94	2.41	0.05	-1.28	6.716	0.91	1.27	10.1	3.17	2.61	0.0249	0.507	107
			[1.93,1.94]	[2.40,2.41]	[-0.03,0.13]	[-1.29,-1.28]	[6.57,6.77]								
	3.5	2.53	3.08	0.61	-1.5	11.21	0.82	1.21	19.7	4.70	3.28	0.0235	0.585	160	
		[2.52,2.53]	[3.08,3.10]	[0.53,0.66]	[-1.55,-1.41]	[11.14,11.26]									
	4.2	2.97	3.56	0.79	-1.53	15.27	0.83	1.5	17.2	5.49	4.50	0.0217	0.583	186	
		[2.96,2.98]	[3.55,3.57]	[0.74,0.82]	[-1.54,-1.52]	[15.24,15.31]									
10	3.0	2.56	3.27	-0.09	-3.56	11.92	0.78	0.95	46.1	3.28	3.92	0.0225	0.551	155	
	[2.56,2.56]	[3.24,3.32]	[-0.19,-0.02]	[-3.70,-3.50]	[11.81,12.15]										
15	3.0	2.52	2.99	0.57	-2.72	10.69	0.84	1.62	46.5	4.11	3.92	0.0225	0.522	139	
	[2.51,2.52]	[2.97,3.00]	[0.435,0.69]	[-2.74,-2.70]	[10.63,10.77]										
0.6	5	3.0	2.66	3.31	0.41	-1.83	12.62	0.80	1.35	16.0	4.48	4.91	0.0212	0.507	147
			[2.65,2.66]	[3.30,3.33]	[0.28,0.49]	[-1.84,-1.82]	[12.57,12.70]								
	3.5	3.11	3.7	-0.10	-1.71	16.46	0.84	1.30	6.5	3.43	4.95	0.0212	0.577	191	
		[3.10,3.11]	[3.67,3.77]	[-0.15,-0.03]	[-1.80,-1.68]	[16.33,17.00]									
	4.2	3.67	4.47	-0.009	-1.24	23.69	0.82	1.33	2.1	3.80	7.11	0.0194	0.577	229	
		[3.65,3.68]	[4.46,4.48]	[-0.04,0.03]	[-1.25,-1.19]	[23.63,23.75]									
10	3.0	2.84	3.49	-0.14	-2.62	14.24	0.81	1.36	19.0	3.45	5.26	0.0209	0.52	160	
	[2.84,2.84]	[3.48,3.49]	[-0.18,-0.08]	[-2.70,-2.59]	[14.21,14.29]										
15	3.0	2.9	3.53	0.77	-2.57	14.73	0.82	1.58	27.7	3.93	5.08	0.0211	0.538	169	
	[2.89,2.91]	[3.52,3.54]	[0.61,0.93]	[-2.58,-2.55]	[14.65,14.79]										
0.8	5	3.0	2.6	3.3	-0.19	-1.34	12.36	0.79	1.33	4.0	3.46	4.04	0.0223	0.553	159
			[2.57,2.64]	[3.29,3.31]	[-0.21,-0.12]	[-1.34,-1.33]	[12.24,12.52]								
	3.5	3.41	4.11	-0.14	-1.5	20.01	0.83	1.37	3.7	3.67	6.13	0.0201	0.571	209	
		[3.40,3.41]	[4.07,4.15]	[-0.24,-0.10]	[-1.54,-1.47]	[19.97,20.10]									
	4.2	4.16	5.11	-0.004	-0.34	30.05	0.81	1.33	1.7	4.02	8.06	0.0188	0.611	273	
		[4.13,4.16]	[5.10,5.11]	[-0.02,0.005]	[-0.37,-0.29]	[29.95,30.22]									
10	3.0	2.98	3.57	0.26	-1.98	15.36	0.84	1.42	10.4	3.73	4.98	0.0212	0.555	178	
	[2.94,2.99]	[3.54,3.58]	[0.15,0.39]	[-2.05,-1.82]	[14.96,15.51]										
1.0	5	3.0	3.02	3.53	0.14	-1.52	15.36	0.85	1.57	9.2	4.67	4.83	0.0213	0.564	181
			[2.98,3.02]	[3.52,3.55]	[0.03,0.19]	[-1.61,-1.47]	[15.18,15.48]								
	3.5	3.84	4.84	0.02	-0.84	26.68	0.78	1.32	1.2	4.12	7.53	0.0191	0.595	251	
		[3.84,3.85]	[4.81,4.86]	[-0.04,0.07]	[-0.87,-0.80]	[26.60,26.73]									
	4.2	4.35	5.36	-0.13	-0.29	33.5	0.81	1.28	0.6	4.22	9.26	0.0181	0.601	284	
		[4.35,4.36]	[5.35,5.38]	[-0.14,-0.09]	[-0.35,-0.25]	[33.34,33.60]									
10	3.0	3.43	4.25	0.15	-2.51	20.92	0.81	1.46	13.7	4.02	6.93	0.0195	0.549	205	
	[3.43,3.44]	[4.22,4.27]	[0.07,0.28]	[-2.53,-2.48]	[20.86,20.96]										
15	3.0	3.64	4.45	-0.27	-3.28	23.28	0.83	1.40	18.2	3.93	7.00	0.0194	0.577	227	
	[3.63,3.64]	[4.44,4.46]	[-0.37,-0.16]	[-3.31,-3.24]	[23.23,23.32]										

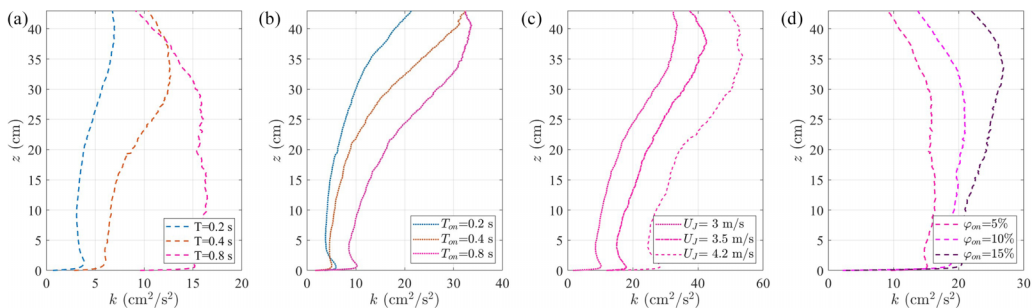


FIG. 3. Profiles of horizontally averaged k for (a) 8×8 RJA, $U_J = 4.2$ m/s, and $\varphi_{\text{on}} = 5\%$, (b) 16×16 RJA, $U_J = 3.0$ m/s, and $\varphi_{\text{on}} = 5\%$, (c) 16×16 RJA, $\varphi_{\text{on}} = 5\%$, and $T_{\text{on}} = 0.8$ s. (d) 8×8 RJA, $U_J = 4.2$ m/s, and $T_{\text{on}} = 0.8$ s. The notation (- -) represent cases with $U_J = 4.2$ m/s, (-.) represents $U_J = 3.5$ m/s, and (..) represents $U_J = 3.0$ m/s. For cases with $\varphi_{\text{on}} = 5\%$, $T_{\text{on}} = 1$ s is denoted by —, $T_{\text{on}} = 0.8$ s is denoted by —, $T_{\text{on}} = 0.6$ s is denoted by —, $T_{\text{on}} = 0.4$ s is denoted by —, $T_{\text{on}} = 0.2$ s is denoted by —. From $\varphi_{\text{on}} = 5\%$ to 15% , the colors get darker.

B. Characteristics of the turbulent region

To estimate the location where the homogeneous region begins, we use the homogeneity deviation, $\mathcal{H}\mathcal{D} = 2\sigma/k^{1/2}$ as in Refs. [25,32], where σ represents the spatial standard deviation of the root mean square velocities in the horizontal direction. A factor of two is included in the formulation of $\mathcal{H}\mathcal{D}$ to ensure 95% of the data falls within the specified range. At the minimum location from the jet array where $\mathcal{H}\mathcal{D} < 0.10$, turbulence can be assumed to be homogeneous. In our experiments, homogeneity is achieved at a distance of $5S-7S$ in most cases, consistent with the observations of Refs. [1,33]. The consistency among different studies confirms the importance of the geometric jet spacing within an RJA with regard to finding a minimum distance at which homogeneity can be achieved. It was observed that at high φ_{on} (i.e., lower S_e), a greater distance is required for the flow

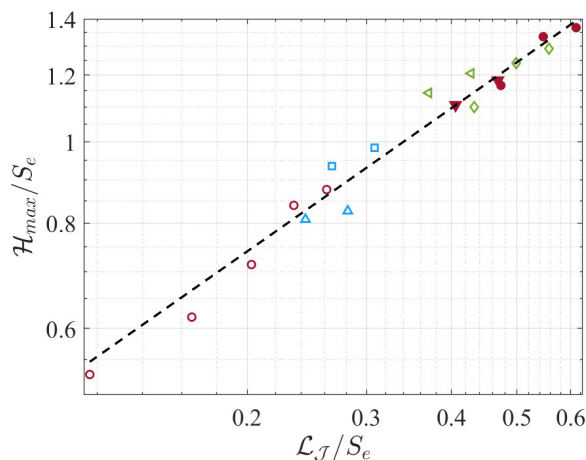


FIG. 4. Dependence of \mathcal{H}_{max} on $\mathcal{L}_{\mathcal{J}}$ in nondimensional form, with logarithmic best-fit curve; burgundy circles, blue squares, and green diamonds represent cases with $\varphi_{\text{on}} = 5\%$, 10% , and 15% respectively with $U_J = 4.2$ m/s. Burgundy downward-pointing, blue upward-pointing triangles and green leftward-pointing triangles represent cases with $\varphi_{\text{on}} = 5\%$, 10% , and 15% respectively, with $U_J = 3.5$ m/s. Filled markers represent the 16×16 RJA, and the unfilled markers represent the 8×8 RJA configuration. The dashed black line is the linear fit to $a(\mathcal{L}_{\mathcal{J}}/S_e)^b$, where $a = 1.8$ and $b = 0.56$.

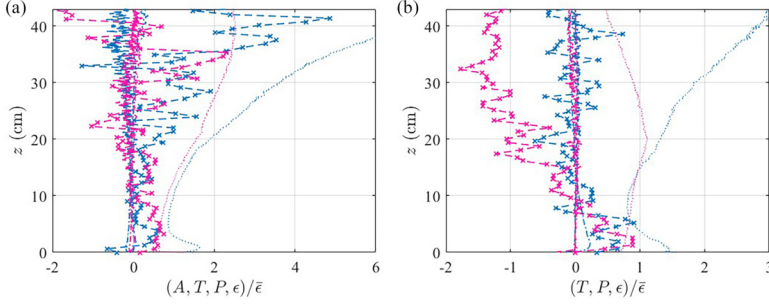


FIG. 5. Normalized profiles of horizontally averaged T , P , A , and ϵ for (a) 16×16 RJA with $U_J = 3.0$ m/s, $\varphi_{\text{on}} = 5\%$ for $T_{\text{on}} = 0.2$ s with $M^* = 46.7\%$, and for $T_{\text{on}} = 0.8$ s with $M^* = 4.0\%$; and (b) 8×8 RJA with $U_J = 4.2$ m/s and $\varphi_{\text{on}} = 5\%$ for $T_{\text{on}} = 0.2$ s with $M^* = 51.7\%$ and for $T_{\text{on}} = 0.8$ s with $M^* = 2.4\%$. $T_{\text{on}} = 0.8$ s is shown by --- and $T_{\text{on}} = 0.2$ s is shown by - - - . The notation (---) represents A , $(\text{-}\times\text{-})$ represents T , $(\text{-}\cdot\text{-})$ represents P , and $(\text{-}\cdot\text{-})$ represents ϵ .

to achieve homogeneity. The location where $\mathcal{HD} < 0.10$ was not affected by M^* ; thus, it can be concluded that the strength of the mean flow does not impact homogeneity.

The role of the mean flow on turbulence statistics, due to spatial gradients within the velocity field, can effectively be assessed by analyzing the steady-state turbulent kinetic energy budget [Eq. (2)]. Here, we compute advection ($A = \langle U_i \rangle \frac{\partial k}{\partial x_i}$), transport ($T = \frac{\partial \langle u_j u_j u_i \rangle}{\partial x_i}$), production ($P = -\langle u_i u_j \rangle \frac{\partial U_i}{\partial x_j}$), and dissipation [$\epsilon = 2\nu \langle s_{ij} s_{ij} \rangle$, where $s_{ij} = \frac{1}{2}(\frac{\partial u_i}{\partial x_j} + \frac{\partial u_j}{\partial x_i})$ is the strain rate]. We do not evaluate terms related to molecular viscous transport ($2\nu \frac{\partial \langle u_j s_{ij} \rangle}{\partial x_i}$) because its magnitude is negligible, or pressure ($\frac{1}{\rho_0} \frac{\partial \langle u_i p \rangle}{\partial x_i}$), as no *in situ* measurements are taken:

$$\langle U_i \rangle \frac{\partial k}{\partial x_i} + \frac{1}{\rho_0} \frac{\partial \langle u_i p \rangle}{\partial x_i} + \frac{1}{2} \frac{\partial \langle u_j u_j u_i \rangle}{\partial x_i} + \langle u_i u_j \rangle \frac{\partial \langle U_i \rangle}{\partial x_j} - 2\nu \frac{\partial \langle u_j s_{ij} \rangle}{\partial x_i} + 2\nu \langle s_{ij} s_{ij} \rangle = 0. \quad (2)$$

We determine A , T , P , and ϵ directly from PIV data, following the approach detailed in Johnson and Cowen [2] and assuming radial symmetry. The accuracy in calculating ϵ directly is assessed through the approach presented in Cowen and Monismith [28], which was adopted based on the proposed universal spectrum of Ref. [34]. At our PIV spatial resolution of $5\eta\text{--}6\eta$, 98% of the dissipation can be captured using this method.

The total kinetic energy budget is presented for two extreme cases with high and low mean flow strength (i.e., $M^* > 40\%$ and $M^* < 5\%$). Figures 5(a) and 5(b) show the normalized profiles of advection, production, dissipation rate, and turbulent transport when using the 16×16 and 8×8 RJAs, respectively. All metrics are normalized by the average value of the dissipation rate, $\bar{\epsilon}$ in the standardized turbulent region (to be clarified later in this section). According to Fig. 5, the magnitude of T varies in all four presented cases but does not follow a specific trend with M^* . P and A both have nearly zero values and are also not correlated with the magnitude of M^* . The sum of the terms considered here does not add up to zero and the TKE budget equation cannot be closed; this is consistent with expectations of negligible-mean-flow turbulence, in which any terms based upon mean velocities (or gradients thereof) will be approximately equal to zero, as shown in Johnson and Cowen [2]. However, the pressure term, which is not considered here, might play an important role in closing Eq. (2) [2,35].

Following the approach of Johnson and Cowen [2], we define a standardized turbulent region within the developed turbulent region, for reporting summary turbulence metrics (see Tables I and II). The region spans $1.5\mathcal{L}_L < z < 4\mathcal{L}_L$, where \mathcal{L}_L is the longitudinal integral length scale. The integral length scale, \mathcal{L}_{ij} , the characteristic length scale of the largest eddies, is defined as the integral of the spatial autocorrelation of the fluctuating velocities, $\rho_{ii,j}$, shown in equation (3). In this

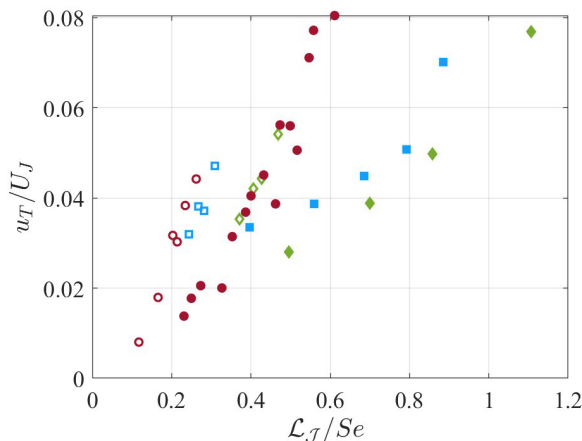


FIG. 6. Variations in the normalized magnitude of u_T (spatially averaged in the FOV) with respect to \mathcal{L}_J/S_e ; burgundy circles, blue squares, and green diamonds represent cases with $\varphi_{\text{on}} = 5\%$, 10% , and 15% respectively. Filled markers represent the 16×16 RJA, and the unfilled markers represent the 8×8 RJA configuration.

equation, X_c denotes the location of the centerline in the j direction, and r_j represents the separation in the j direction. The longitudinal integral length scale is found when $i = j$ (e.g., $\mathcal{L}_L = \mathcal{L}_{ii,i}$), and the transverse integral length scale is denoted by $\mathcal{L}_T = \mathcal{L}_{ii,j}$ when $i \neq j$.

$$\rho_{ii,j} = \frac{\langle u_i(X_c - \frac{r_j}{2})u_i(X_c + \frac{r_j}{2}) \rangle}{[\langle u_i^2(X_c - \frac{r_j}{2}) \rangle \langle u_i^2(X_c + \frac{r_j}{2}) \rangle]^{\frac{1}{2}}}. \quad (3)$$

In our study, due to the narrow FOV, we use exponential fits to $\rho_{ii,j}$, as in Johnson and Cowen [2], to estimate \mathcal{L}_L and \mathcal{L}_T , such that $\rho_L = e^{-r_j/\mathcal{L}_L}$ and $\rho_T = e^{-r_j/2\mathcal{L}_T}(1 - r_j/4\mathcal{L}_T)$.

In the standardized turbulent region, k increases with T_{on} , consistent with the observations of Johnson and Cowen [2]. However, in contrast with Johnson and Cowen [2], we also observe that an increase in φ_{on} corresponds to an increase in k . To better illustrate the variations of k with other input variables, we define a turbulent velocity as $u_T = k^{1/2}$. Figure 6 illustrates the changes in u_T associated with the output flow of individual jets, determined as \mathcal{L}_J/S_e , showing a strong correlation between the turbulent kinetic energy and the output flow of the individual jets. We see that for specified φ_{on} , u_T/U_J increases nearly linearly with \mathcal{L}_J , although specific correlations vary with φ_{on} .

Two different metrics can be used to evaluate the degree of isotropy in turbulent flow [31]. The first, and more common, metric is the ratio of orthogonal RMS velocities, $\Omega = u'/w'$, while the second is the ratio of the longitudinal to the transverse integral length scales, $\Omega_{\mathcal{L}} = \mathcal{L}_L/\mathcal{L}_T$. In isotropic turbulence, Ω should be equal to one and $\Omega_{\mathcal{L}}$ should be equal to two. The average magnitude of both isotropy ratios in the standardized turbulent region varies with the RJA input parameters. Figure 7 shows the average value of Ω and $\Omega_{\mathcal{L}}$ in the standardized turbulent region with regard to \mathcal{L}_J . As can be seen in Fig. 7, values of Ω using the 8×8 RJA are roughly equal to 0.9, compared with roughly 0.8 when using the 16×16 RJA. According to our analysis, the flow exhibits better isotropy in cases with $S = 10$ cm compared with $S = 5$ cm, especially for higher values of φ_{on} . In regards to $\Omega_{\mathcal{L}}$, the flow generated by the 8×8 RJA has values of $\Omega_{\mathcal{L}}$ varying between 1.15 and 2.06 with a median of 1.88, compared with the 16×16 RJA, which varies between 0.93 and 1.89 with a median of 1.37.

Figure 8 demonstrates the variations of M^* in the standardized turbulent region as a function of \mathcal{L}_J/S_e . This figure depicts that for both array configurations, lower T_{on} and higher φ_{on} are associated with higher mean flow. A notable drop in the relative mean flow strength can be observed as U_J and

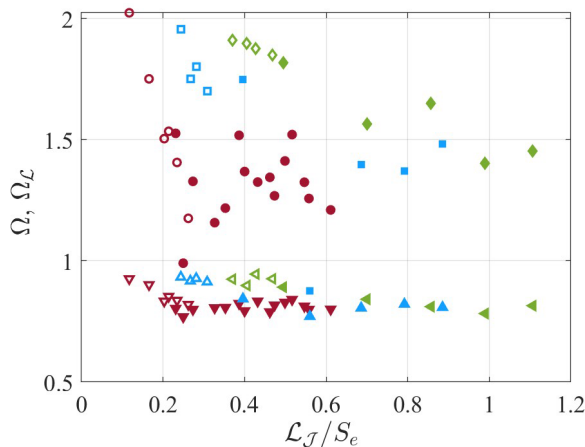


FIG. 7. Average isotropy ratios Ω and Ω_L in the standardized turbulent region with respect to \mathcal{L}_J . For Ω_L , the markers are the same as in Fig. 4. For Ω , burgundy downward-pointing triangles, blue upward-pointing triangles, and green leftward-pointing triangles represent cases with $\phi_{on} = 5\%$, 10% , and 15% respectively. Filled markers represent the 16×16 RJA, and the unfilled markers represent the 8×8 RJA configuration.

T_{on} increase. Interestingly, U_J does not explicitly control M^* , as can be observed prominently in the data provided in Tables I and II. In some cases, such as with the 16×16 configuration for $T_{on} = 0.4$ s, M^* increases with U_J , and in other cases, such as with the 8×8 configuration for $T_{on} = 0.8$ s, M^* decreases as U_J increases (see Table I). These results indicate that the strength of the mean flow is more strongly influenced by the operation time of each jet rather than the output velocity of individual jets.

The magnitudes of ϵ averaged within the standardized turbulent region are reported in Tables I and II. Also, the nondimensionalized value of ϵ is shown in Fig. 9, in which the nondimensionalization is adopted from the analysis of Tan *et al.* [33]. A strong correlation between nondimensional ϵ and normalized jet penetration depth is observed in Fig. 9.

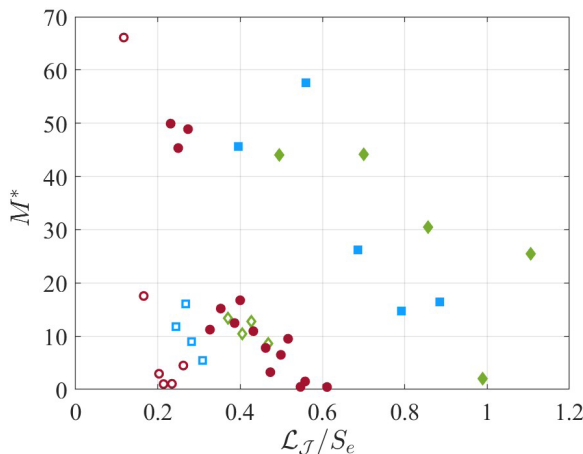


FIG. 8. Variation of M^* (spatially averaged within the standardized turbulent region) with respect to \mathcal{L}_J/S_e . See Fig. 4 for markers and color scheme.

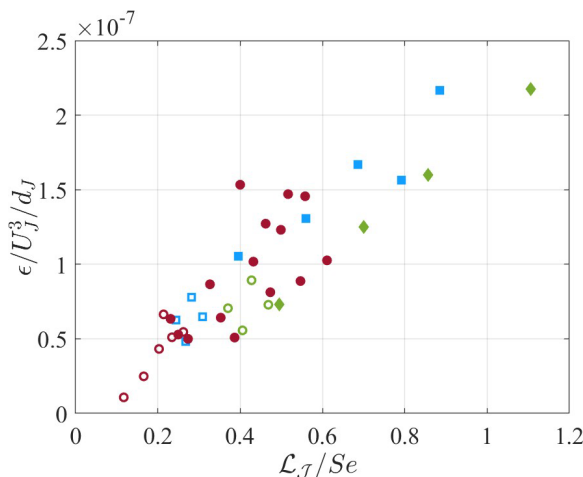


FIG. 9. Variation of ϵ (spatially averaged within the standardized turbulent region) with respect to L_J/S_e . See Fig. 4 for markers and color scheme.

Upon determining the magnitude of ϵ within the standardized turbulent region, other turbulence statistics can be calculated. The Kolmogorov length scale and timescale are calculated as $\eta = (\nu^3/\epsilon)^{1/4}$ and $\tau_\eta = (\nu/\epsilon)^{1/2}$. The Taylor microscale is calculated as $\lambda_g = (15\nu u_T^2/\epsilon)^{1/2}$. Finally, the Reynolds number based on the Taylor microscale is calculated as $\text{Re}_\lambda = u_T \lambda_g/\nu$. The values of these parameters for each case are presented in Tables I and II.

Referring to Tables I and II, we note several trends between the input variables and output statistics of the standardized turbulent region. Increasing T_{on} , U_J , and φ_{on} increases Re_λ , k , and \mathcal{L}_L , and decreases η in almost all cases. Variations of λ_g between cases are small, with $0.466 \text{ cm} < \lambda_g < 0.611 \text{ cm}$. In almost all cases, an increase in U_J and φ_{on} increases λ_g . In the explored range of φ_{on} , an increase in φ_{on} results in an increase in M^* in almost all cases, whereas the effects of T_{on} and U_J on M^* do not show a specific trend.

C. The decay of turbulence

After the turbulent flow enters the fully developed state (recall, $\mathcal{H} > \mathcal{H}_{\text{max}}$) turbulence decays with distance from the jet array. Turbulence decay can be studied from the variations in both k and ϵ . Here, we focus on the decay of k . Based on existing experimental, theoretical, and computational studies on the decay of turbulence [10,36,37], u_T follows a power-law when it decays, similar to

$$u_T \propto \mathcal{H}^{-n}, \quad (4)$$

where n is the decay exponent and \mathcal{H} is distance from the jet array. Figure 10 presents profiles of u_T nondimensionalized by U_J , with respect to \mathcal{H} along with linear fits that satisfy Eq. (4) in selected regions of the profiles, in order to illustrate the decay of u_T/U_J with distance from the jet array with different variables. Based on our analysis, the value of n varies across different tests (i.e., different parameter combinations) and even within tests at different locations in the measurement region. The cases are grouped to demonstrate specific scenarios across all decay regions identified.

We have identified three distinct decay regions (see Fig. 11)—a transitional region, a near-field region, and a rapid decay region. In each case, a combination of one or multiple decay regions was observed. The first region, situated immediately below \mathcal{H}_{max} , is where the flow transitions from turbulence production-dominant to decay-dominant. This region, where $n < 1$, varies in size depending on the RJA inputs (e.g., T_{on} , φ_{on} , U_J , and S). In some cases, this region is relatively short [i.e., Fig. 10(a); $T_{\text{on}} = 0.2 \text{ s}$], while in other cases it extends further from the RJA [i.e., all cases

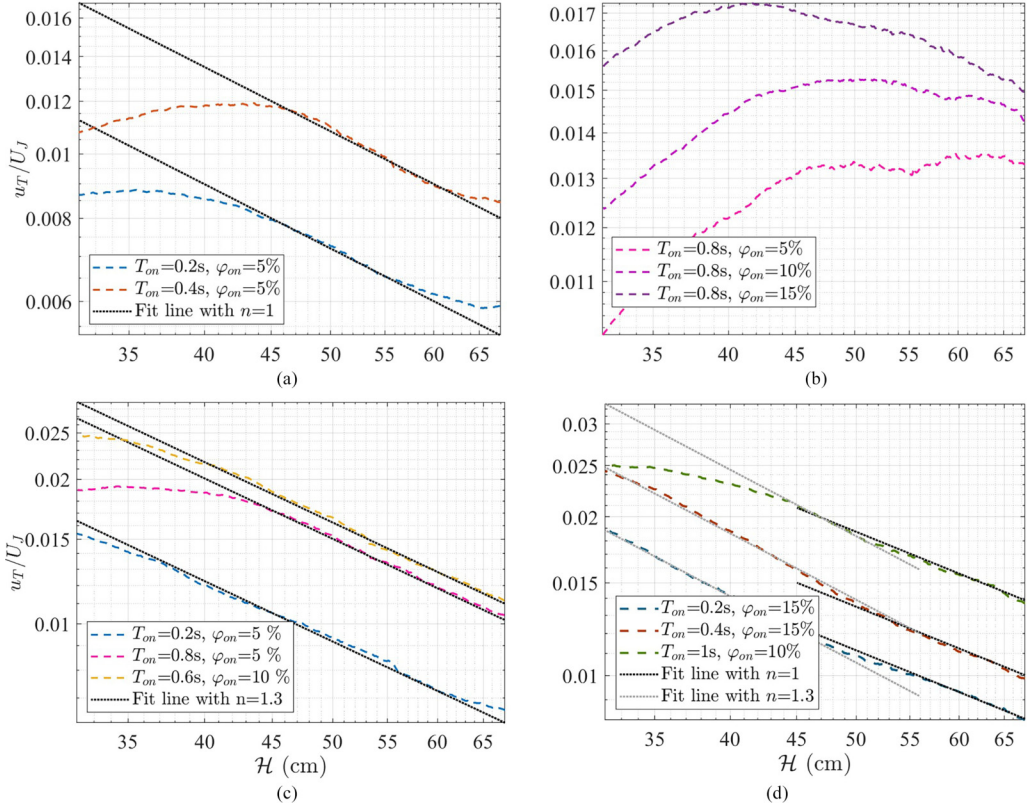


FIG. 10. Logarithmic plot of k with respect to distance from the RJA, \mathcal{H} , for (a) 8×8 RJA, $U_J = 4.2$ m/s, and $\varphi_{on} = 5\%$; (b) 8×8 RJA, $U_J = 4.2$ m/s; (c) 16×16 RJA, $U_J = 3$ m/s; and (d) 16×16 RJA, $U_J = 3$ m/s, and $T_{on} = 0.8$ s.

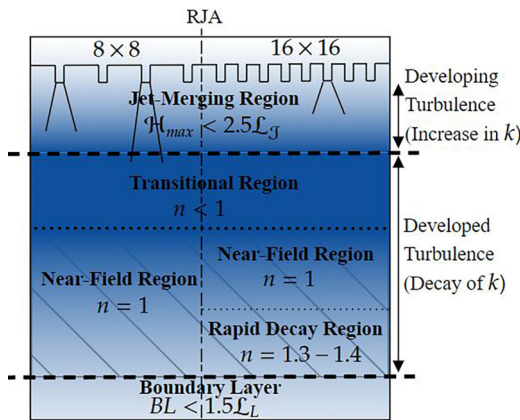


FIG. 11. Different regions of development and decay of turbulence in an RJA facility. The inclined hatched lines mark the regions that may or may not be present based on the input parameters of the RJA. The vertical dashed line separates the 8×8 and 16×16 RJAs.

in Fig. 10(b)]. In Fig. 10(b), a nearly flat profile of k can be observed below \mathcal{H}_{\max} for $\varphi_{\text{on}} = 5\%$, signifying an extended transitional region.

Following the transitional region is a region that closely resembles the “near-field” decay region in grid-generated wind and water tunnels [38]. In this region, which is observed in both array configurations, u_T decays with $n = 1$ [see Figs. 10(a) and 10(d)]. Finally, a region characterized by higher decay rates, with $1.3 < n < 1.4$, was observed in some trials with the 16×16 RJA. This region can occur either immediately after the transitional region or after the near-field region [see Figs. 10(c) and 10(d)]. While the region after the near-field region in the grid-generated wind and water tunnel facilities (i.e., the “far-field” region) has lower decay rates compared with the near-field region, the rapid-decay region in our facility has higher decay rates compared with the near-field region with RJAs. This makes the decay in RJA facilities different from that in grid-generated wind and water tunnels. In grid turbulence, the decay rate decreases by moving away from the grid until it reaches its final decay region. By contrast, with RJAs, the decay rate of turbulence increases with distance from the jet array. This might be due to the activity of pumps entering and extending further into the facility and the turbulence being confined by the boundaries [15,32].

The discrepancy between the decay of turbulence in wind and water tunnels and RJA facilities is due to the mechanisms of generation of turbulence, as mentioned in Ghazi Nezami *et al.* [15]. The value of n is a result of the balance between the production and the dissipation of turbulence; depending on the region in the facility, this balance changes. Unlike decay of grid-generated turbulence in wind and water tunnels where the decay follows $\epsilon = dk/dt = \langle U \rangle dk/dx$ [39,40], this cannot be applied to RJA facilities as the mean flow is a function of distance from the jet array, and its value is negligible in many cases. Additionally, the majority of the turbulence generated in wind and water tunnels is due to the interaction of wakes generated by the grids, which diminishes with distance from the grids. By contrast, in RJA facilities, turbulence generation is more present throughout the height of the facility.

In contrast with prior studies employing planar jet arrays that suggest a single value for n [11,33], we emphasize that this is not consistent with our findings. Our data suggest the spatial decay of turbulence from an RJA experiences different stages with unique n (see, e.g., Ref. [40]), and the extent and characteristics of these regions depend on the input momentum in the system (e.g., input parameters to the RJA) [38]. According to Fig. 10, the strength of the mean flow does not impact the decay of turbulence, as these decay trends are observed across a wide range of M^* . A recent review by Ghazi Nezami *et al.* [15] noted that in RJA facilities, the decay of turbulence does not have a counterpart to the far-field region of wind and water tunnels with grid-generated turbulence; this study has strengthened this claim. Due to spatial constraints within RJA-driven facilities (e.g., limited distance between RJAs and boundaries), it may not always be feasible to observe all stages of decay, but it is possible to have multiple decay regions.

IV. INPUT ENERGY AND THE GENERATED TURBULENCE

Thus far, we have investigated how unique combinations of the RJA input variables affect the production (and subsequent dissipation) of k , the presence of mean flows, and other turbulence characteristics. In this section, we aim to synthesize the combinations of input parameters so that we may explore the relationship between the cumulative energy supplied to the system (E_t) with the resultant turbulent flow. While we did not find the strength of mean flows to affect the production of turbulence (recall Sec. III A), we restrict our analysis in this section to cases for which $T_{\text{on}} = 0.6, 0.8, 1.0$ s due to these trials mostly having $M^* < 5\%$, with a few cases showing M^* between 5% and 20% (recall Tables I and II). Our aim is to predict the energy balance in the standardized turbulent region (recall Sec. III B).

To estimate the input energy, it is necessary to consider the algorithm that controls pump operation. Explicitly, the algorithm uses inputs φ_{on} and T_{on} . While T_{on} determines the duration of operation for each pump, φ_{on} controls the percentage of time over which an individual jet injects momentum, and T_{on} is encapsulated within φ_{on} . Hence, the input energy should be proportional to

φ_{on} and independent of T_{on} . Another factor that contributes to the energy input from the RJA is the total number of jets, N . Finally, the amount of energy input from an individual jet, which is proportional to U_J^2 , directly contributes to the total input energy. Therefore, E_t can be estimated based on equation (5):

$$E_t \propto U_J^2 \varphi_{\text{on}} N. \quad (5)$$

E_t is then distributed throughout the tank, and transfers away from the jet array. This energy is divided into two forms—mean and turbulent kinetic energy—and eventually dissipates via viscosity due to local and instantaneous fluid shear and at physical boundaries of the tank. It should be noted that Eq. (5) does not include the jet cross-sectional area, an important factor in the input energy from individual jets, as d_j is the same in all experiments.

Shortly after initiating the turbulence generation process, the system reaches a statistically stationary state, and E_t balances out with total energy dissipation in the entire facility. Therefore, in the turbulent region, k and ϵ are direct consequences of E_t , as was observed in Sec. III B. Therefore, both k and ϵ are functions of U_J , φ_{on} , and N . The relation $\epsilon = 15\nu u_T^2/\lambda_g^2$ [31] provides a direct link between ϵ and k . As stated in Sec. III B, the variations in λ_g are small—below 19% in cases considered here. According to the review of Ghazi Nezami *et al.* [15], it is true that in all HIT-generating facilities such as RJAs, the turbulent length scales are dominantly influenced by the physical properties of facilities more so than algorithmic parameters. Therefore, $\epsilon \propto k$, and consequently they should exhibit similar relationships with U_J , φ_{on} , and N .

We first consider how k is a function of the RJA inputs. The relationship describing k is not as straightforward as for E_t . We propose equation (6) for k :

$$k \propto U_J^{a_k} \varphi_{\text{on}}^{b_k} N^{c_k}, \quad (6)$$

in which the values of a_k , b_k , and c_k , the exponents of each contributing parameter, will be evaluated from measurements collected in the standardized turbulent region.

To explore how U_J affects the flow downstream of an array of jets, we utilize the study of Aleyasin and Tachie [41] regarding variations of Re_j in twin jet setups. According to this study, changes in Re_j do not alter the mean velocity and Reynolds stress profiles; at a specific distance from the outlet, the combined flow of twin jets is similar to that of a single jet. Similarly for twin synthetic jets, Greco *et al.* [42] showed that the profile of centerline velocity downstream of the merged flow is comparable to the profile of a single jet, especially for cases in which $S \geq 3d_j$. Based on these studies, we hypothesize that in RJA-driven turbulence, k is correlated with U_J^2 , and therefore we propose that in Eq. (6), a_k should be equal to two. We test this by finding the slope of the logarithmic plot of k with U_J , when φ_{on} , N , and T_{on} are kept constant. The result shows that on average, $a_k = 2.14$ across test cases, which is close to our estimation.

The relationship between the total and the average operating number of jets in the RJA and the input energy is more difficult to estimate. One reason for this is that as N changes, S changes in turn, provided the distribution of jets occupies a fixed footprint. Similarly, as φ_{on} increases, S_e decreases—and vice versa. Despite the complexity of our system, we hypothesize that b_k and c_k must be less than one, based on studies of superposition of jets (see, e.g., Ref. [41]). Using our experimental data, we determine the values of these two exponents using a similar approach as finding a_k . We consider $k/U_J^{a_k}$ as a function of φ_{on} for different values of T_{on} using both array configurations and determine b_k as the average slope. The same process has been adopted for determining c_k , in which we explore the relationship between $k/U_J^{a_k}$ and $N\varphi_{\text{on}}^{b_k}$ for each T_{on} , with known a_k and b_k .

Estimates of b_k and c_k are presented in Table III. The estimated values of b_k and c_k are the same for both array configurations. By comparing the values of b_k and c_k in Eq. (6), we gain an understanding of how the input energy converts to the output values (i.e., turbulence metrics), an example of which is shown in Fig. 12 for turbulent kinetic energy. In this figure, it can be seen that all values with the same T_{on} collapse accordingly.

Notice that in the explanation presented above, we neglected T_{on} for predicting k in the standardized turbulent region. However, Carter *et al.* [25] and Johnson and Cowen [2] showed that changing

TABLE III. Estimated values of the exponents of the proposed power-law for predicting k , ϵ , and Re_λ ; a , b , c are the exponents and subscript i refers to k , ϵ , and Re_λ .

Parameter	k	ϵ	Re_λ
a_i	2.14	1.9	1.37
b_i	0.3	0.38	0.14
c_i	0.45	0.42	0.22

T_{on} directly affects k . Since the mean and turbulent kinetic energy both are derived from the input energy, their ratio varies based on the forms of interactions and routes of energy transfer in the tank. At very low T_{on} , the pump outlet flow is brief in duration and small in width (i.e., lateral spread in x and y), similar to a pulsating synthetic jet [43]. Additionally, as T_{on} shortens, the probability of direct interaction between two jets decreases. As T_{on} increases, the behavior of each individual jet deviates more from the conventional pulsating synthetic jet behavior toward that of a continuous synthetic jet, and the stochastic nature of the setup is diminished. With increasing T_{on} , the signature of the outlet flow of each pump extends farther in the tank with longer \mathcal{L}_J , increasing the possibility of interactions of jets with one another and with the ambient flow.

Based on the presented argument, we expect to see a steep increase in k with T_{on} at relatively small T_{on} within a certain range; as T_{on} continues to increase, the rate of change in k will decrease until it ultimately reaches a saturation point at a critical on-time, $T_{\text{on-cr}}$, beyond which no further changes would be expected for k . Carter *et al.* [25] tested T_{on} across a wide range, and we evaluate this argument using their data. Data presented in the study of Carter *et al.* [25], shown in Fig. 13, illustrate an asymptotic behavior between the reported k values for each case (normalized by the maximum values of k that were achieved for specific configurations), as $T_{\text{on}} \rightarrow \infty$. Based on Fig. 13, we propose that k increases as follows:

$$\frac{1}{2} + \frac{1}{2} \text{erf} \left(c_0 \frac{T_{\text{on}}}{T_{\text{on-cr}}} \right).$$

We test this hypothesis by fitting the error function to the data of Carter *et al.* [25] for each configuration, and we observe good agreement between the predicted and measured values. Based on our analysis, S is not strictly influential on c_0 . However, inserting a grid immediately downstream of the jet orifices halves the values of c_0 . Additionally, the total number of operating jets directly influences k_{max} . φ_{on} was constant in their studies, therefore its effect on c_0 cannot be evaluated.

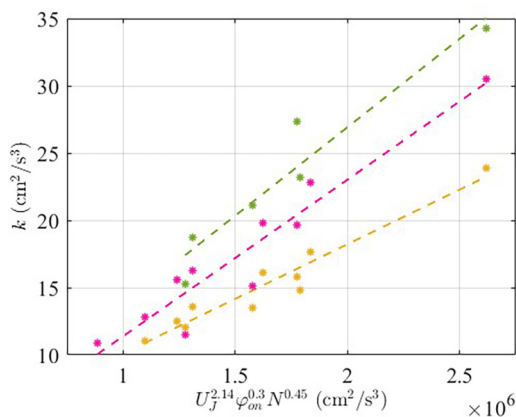


FIG. 12. Correlation between k and $N^{b_k} \varphi_{\text{on}}^{c_k} U_J^{a_k}$, with b_k and c_k values presented in Table III.

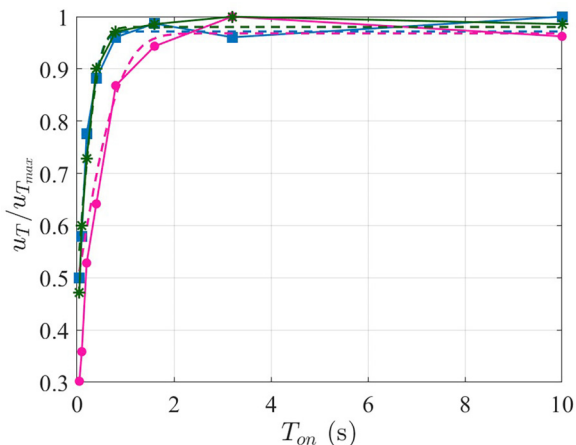


FIG. 13. Normalized u_T with respect to T_{on} in the study of Carter *et al.* [25] for baseline configuration (squares, blue), after inserting grid (circles, pink), and after doubling the jet spacing (stars, green). The solid lines represent the data and the dashed lines represent the fitted functions, in matched colors.

As mentioned at the beginning of this section, ϵ and k are similarly affected by the input energy to the system. Tan *et al.* [33] proposed that the dissipation rate with a jet array (recalling that their facility has continuous, not stochastic, forcing) scales as $\epsilon \propto U_J^3/d_J$. However, this relationship does not encompass all of the aspects that contribute to the input energy in our setup (i.e., φ_{on} and N). Additionally, since d_J is uniform for all cases in our study, we cannot quantify its effect independent of U_J . Following our methodology for estimating k in regard to the input energy, we repeat the same process for ϵ with equation (7):

$$\epsilon \propto U_J^{a_\epsilon} \varphi_{on}^{b_\epsilon} N^{c_\epsilon}. \quad (7)$$

We find $a_\epsilon = 1.9$, which is close to our prediction of $\epsilon \propto U_J^2$, stemming from $\epsilon \propto k$ and $k \propto U_J^2$, rather than $\epsilon \propto U_J^3$ proposed by Tan *et al.* [33]. With $\epsilon \propto U_J^{a_\epsilon}$, we find values of b_ϵ and c_ϵ are similar to b_k and c_k (Table III), further showing the strong coupling between k and ϵ .

Using Eqs. (6) and (7) for k and ϵ , respectively, we propose a relationship linking Re_λ (i.e., $Re_\lambda = \frac{20}{3} Re_L^{1/2}$, where $Re_L = \frac{k^2}{\epsilon \nu}$ [31]) with the input parameters of the RJA, (N , φ_{on} , and U_J), using the exponent values presented in Table III. The resultant relationship is $Re_\lambda \propto U_J^{1.19} \varphi_{on}^{0.17} N^{0.22}$. We then follow the same methodology as used for k and ϵ to determine the exponent values for Re_λ from our data. As can be seen in Table III, the exponents determined from the data by first finding a_{Re} , and then b_{Re} and c_{Re} closely match those found when we substitute k and ϵ into the Re_λ relationship. Figure 14 depicts the estimated relationship with the exponent values.

We propose a variable Γ to assess the efficiency of our setup as a function of input variables. Two distinct methodologies can be employed to compute Γ , each elucidating different aspects of the system performance. In the first approach, Γ_p is found by dividing ϵ by the input power supplied to the facility. The total input power is calculated as $P_{in} = IVN\varphi_{on}$, where I and V are the current and voltage supplied to the pumps. To ensure consistency between the dissipation rate (i.e., cm^2/s^3) with the input power (i.e., watts), we multiply $\bar{\epsilon}$ by the mass of water within the extended turbulent region. As indicated by Bellani *et al.* [44], the turbulence retains its homogeneity at a distance of two integral scales from the walls, specifically in planes parallel to the input forcing. Therefore, we take the extended turbulent region to have the same height as the standardized turbulent region (i.e., $4\mathcal{L}_L - 1.5\mathcal{L}_L$), and a lateral footprint that covers the central region of the tank, up to $2\mathcal{L}_L$ from the walls. The input power, P_{in} , is adjusted to correspond to the extended turbulent region such that we multiply P_{in} by the volume of the extended turbulent region and divide it by the total volume of

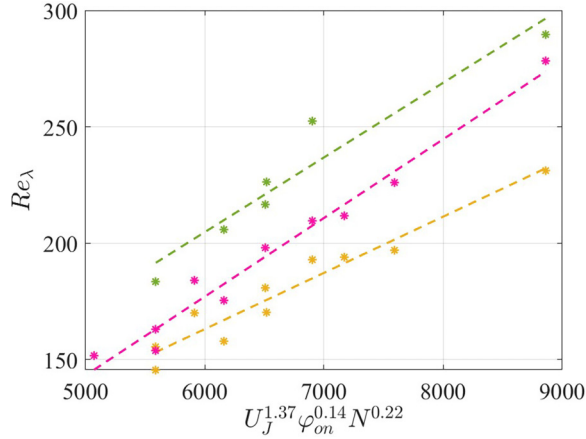


FIG. 14. Variation of Re_λ with $U_J^{a_{Re}} N^{b_{Re}} \varphi_{on}^{c_{Re}}$. See Fig. 3 for color scheme.

the facility. Therefore, after simplifying, the efficiency is calculated as $\Gamma_P = V_T \rho \epsilon / P_{in}$, where $V_T = 84 \times 84 \times 72 \text{ cm}^3$ is the total volume of water between the jet orifice plane and bottom boundary, and ρ is the density of water. The result of Γ_P calculated from this technique is shown in Fig. 15.

Alternatively, Γ_E is computed via dividing the mean value of k measured in the standardized turbulent region by E_t . We normalize k and E_t based on their best representative volume. We assume k is constant across the extended turbulent region, with a height corresponding to the height of the turbulent region; this assumption is consistent with considerations of radial symmetry and homogeneity in this region. Therefore, we normalize k (per unit volume) by dividing its average magnitude within the standardized turbulent region (recall Tables I and II) by the aforementioned volume dimensions. To normalize E_t , we divide the magnitude of E_t [calculated from Eq. (5)] by the total volume of the facility, V_T . This method of finding Γ_E produces nearly identical results to Γ_P , despite its markedly different approach.

According to the results obtained for Γ_P (shown in Fig. 15), the majority of the turbulence is dissipated outside of the extended turbulent region (e.g., at the walls or the jet merging region), due to noticeably higher velocity gradients. Thus, in RJA systems, significant input power is necessary to achieve comparable levels of k in the turbulent region. Figure 15 demonstrates the correlation

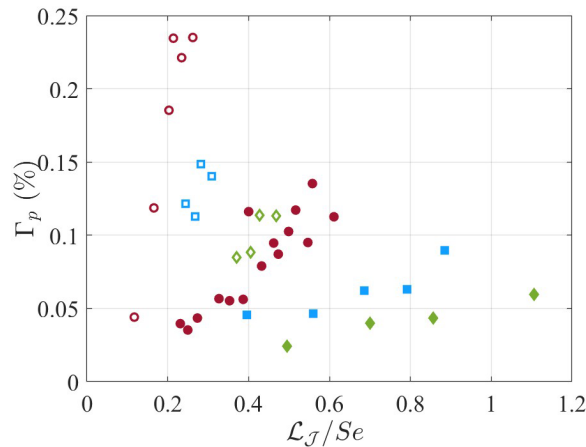


FIG. 15. Variation of Γ_P with respect to \mathcal{L}_J / Se . See Fig. 4 for markers and color scheme.

between input variables and the efficiency of turbulence generation. Increasing T_{on} and U_J more significantly impact efficiency for the less dense array (i.e., 8×8 RJA, which both has a smaller number of operating jets and increased spacing between the jets). This can be seen via the variations of Γ within each marker, which specifies a specific φ_{on} and RJA configuration and corresponds to a particular average number of active jets (i.e., $N\varphi_{\text{on}}$). The lower the values of φ_{on} and N , the higher the rate of increase in Γ_P with increasing T_{on} and U_J . The smallest T_{on} (i.e., 0.2 s; the lowermost points within each cluster of φ_{on}) has the lowest efficiency for all combinations of input variables. The lowest values of Γ are also associated with the highest magnitudes of mean circulation in these cases (recall Tables I and II). Another observation is that increasing φ_{on} results in abrupt decreases in Γ_P . While our data show that increasing φ_{on} is associated with an increase in k , our analysis of Γ_P indicates that this is not the most efficient way to increase k , relative to the other RJA controls. However, as mentioned earlier, increasing T_{on} to achieve higher values of k , while a common practice, is also only effective up to a certain limit.

V. DISCUSSION AND CONCLUSIONS

In this study, we addressed the evolution of turbulence in RJA facilities. The main questions concerned with the flow characteristics and energy transfer in these facilities are the following:

- (1) How do the input variables of the system affect the evolution of the flow in a facility equipped with an RJA? How do flow characteristics, such as isotropy, homogeneity, and mean circulations vary in the developed turbulent region in the facility?
- (2) How can we characterize trends of development and decay of turbulence?
- (3) Is it possible to connect the input energy (based on the input variables) of the system to the energy of the resulting flow?

These questions were investigated by performing a series of experiments in an RJA facility using two different array configurations with different S , while concurrently altering T_{on} , φ_{on} , and U_J .

In most cases within our study, the flow transitions to a homogeneous state at a distance $\leq 6S$ from the jet array, aligned with the findings of previous studies. It was observed that the strength of the mean flow, as measured by M^* , does not affect the homogeneity in the generated flow, as homogeneity is satisfied in most of the cases studied despite significant variation of M^* . In addition to homogeneity, we also investigate the effects of M^* on the turbulent kinetic energy budget in the generated flow. The terms considered include production, transport, advection, and dissipation. We compared cases of high and low M^* , and we observed the impact of the strength of the mean flow on the production, advection, and transport of turbulence in our setup is negligible.

A standardized turbulent region is defined, satisfying homogeneity, and is used for comparing turbulence statistics among cases. We study isotropy and mean flow strength, among other turbulence statistics in this region. The isotropy variables Ω and $\Omega_{\mathcal{L}}$ within the standardized turbulent region change with the input variables. The flow is closer to isotropic turbulence at lower T_{on} compared with higher T_{on} . The magnitude of $\Omega_{\mathcal{L}}$ is more sensitive than Ω to changes to the input variables. The strength of the mean flow is lower for smaller φ_{on} in both array setups. At lower T_{on} and higher φ_{on} , M^* values are large, and the mean kinetic energy can be equivalent to the turbulent kinetic energy (e.g., for $T_{\text{on}} = 0.2$ s). If it is desired to achieve low mean flow HIT, reducing T_{on} is not necessarily a suitable approach. Additionally, solely changing U_J does not guarantee a reduction in M^* . Thus, a careful selection of input variables is useful while aiming to generate high Reynolds number isotropic turbulence with a negligible mean flow.

As is evident from the analysis presented in Sec. III, the flow in the tank is partitioned into different sections representing regions where k develops and where it decays (recall Fig. 11). By moving away from the jet array, k increases up to a certain point, \mathcal{H}_{max} . \mathcal{H}_{max} is dependent on the input variables of the system and increases as normalized jet penetration depth increases in the jet-merging region. We found $\mathcal{H}_{\text{max}} < 2.5\mathcal{L}_{\mathcal{J}}$ in all of our experiments. Once k reaches its fully developed state (beyond \mathcal{H}_{max}), it enters the transitional region where the rate of decay increases, eventually reaching a maximum decay rate. The transitional region using both RJAs may

be followed by a region called the near-field region, where a decay rate of $n = 1$ is observed. In our studies, we found that turbulence decays differently whether using the 8×8 or 16×16 RJA. In some cases of the 16×16 RJA, a rapid decay region with $1.3 < n < 1.4$ was observed, which can follow the near-field region or can be present immediately after the transitional region. This is the first study highlighting the vertical variability of turbulence decay rates in an RJA facility and the dependence of these decay rates on the input variable of the system. Given this new finding, there is great advantage in continued experiments on decay.

We provide an analysis of the energy distribution in RJA facilities. We propose the input energy into the system, E_t , is determined by the total number of jets that are, on average, operating, along with the energy that each jet is inputting to the system. The former is correlated with $N\varphi_{\text{on}}$, and the latter is correlated with U_J^2 . In the mean flow free turbulent region, the output energy of the flow, which is mainly k , is influenced by the same parameters as E_t . Therefore, N , φ_{on} , and U_J are found to directly contribute to k via a power-law. The exponents of this relationship are calculated using the laboratory data. Based on the same argument, relationships for estimating ϵ and Re_λ are found. Although we acknowledge that the power-law values in the relationships presented for estimating flow metrics might not be universal, they provide valuable insight regarding the energy distribution within these facilities. We note that T_{on} has been hypothesized to have no contribution to E_t as it is embedded in φ_{on} . However, it was observed that T_{on} affects k following an error function relationship.

Finally, we define the parameter Γ as an estimate of the efficiency of turbulence generation due to the combination of input variables. This is achieved via two routes. The first method compares the ratio of the power input to the system via pumps to the dissipation rate of the output flow in an extended turbulent region, and the second method compares the magnitude of the total input energy of the flow to turbulent kinetic energy. Both of these techniques result in very similar patterns and values for Γ . At low T_{on} and high φ_{on} , Γ is consistently low. Even though higher T_{on} and U_J are linked with an increase in Γ , increasing φ_{on} has a negative impact on how much T_{on} and U_J can increase Γ . While it may seem intuitive that all of the forced jet flows will lead directly to the production of k (with subsequent dissipation due to high instantaneous shear at the boundaries), especially given how much control we have over turbulence statistics based on modifications to the RJA input parameters, we recall that if we compare turbulent kinetic energy with input jet velocities via the ratio u_T/U_J (recall Fig. 6), this ratio is on the order of 0.1. Thus, there is clearly not a 1 : 1 balance between the RJA forcing and resultant k . We find that only 0.1% of the input energy to the system, as defined either within E_t or P_{in} , ultimately transitions to turbulence.

ACKNOWLEDGMENTS

We graciously acknowledge financial support provided by the National Science Foundation under Award No. CAREER-2236654, along with financial support from a Research Creative Grant provided by the University of Texas at Austin Office of the Vice President for Research. We also acknowledge Evan Variano and Rui Ni for motivating early discussions regarding the distance from the RJA at which the flow transitions to HIT. Finally, we kindly thank two anonymous reviewers for providing valuable feedback and engaging commentary to support improvements to this paper.

-
- [1] E. A. Variano and E. A. Cowen, A random-jet-stirred turbulence tank, *J. Fluid Mech.* **604**, 1 (2008).
 - [2] B. A. Johnson and E. A. Cowen, Turbulent boundary layers absent mean shear, *J. Fluid Mech.* **835**, 217 (2018).
 - [3] E. J. Hopfinger and J.-A. Toly, Spatially decaying turbulence and its relation to mixing across density interfaces, *J. Fluid Mech.* **78**, 155 (1976).

- [4] M. Byron, J. Einarsson, K. Gustavsson, G. Voth, B. Mehlig, and E. Variano, Shape-dependence of particle rotation in isotropic turbulence, *Phys. Fluids* **27**, 035101 (2015).
- [5] A. McCutchan, The development of an experimental apparatus to investigate ice melting rates via homogeneous isotropic turbulence, Master's thesis, The University of Texas at Austin, 2020.
- [6] T. Uzkan and W. Reynolds, A shear-free turbulent boundary layer, *J. Fluid Mech.* **28**, 803 (1967).
- [7] N. Thomas and P. Hancock, Grid turbulence near a moving wall, *J. Fluid Mech.* **82**, 481 (1977).
- [8] D. Aronson, A. V. Johansson, and L. Löfdahl, Shear-free turbulence near a wall, *J. Fluid Mech.* **338**, 363 (1997).
- [9] H. Rouse and G. Dodu, Turbulent diffusion across a density discontinuity, *Houille Blanche* **10**, 530 (1955).
- [10] S. Thompson and J. Turner, Mixing across an interface due to turbulence generated by an oscillating grid, *J. Fluid Mech.* **67**, 349 (1975).
- [11] E. A. Variano, E. Bodenschatz, and E. A. Cowen, A random synthetic jet array driven turbulence tank, *Exp. Fluids* **37**, 613 (2004).
- [12] S. Bounoua, G. Bouchet, and G. Verhille, Tumbling of inertial fibers in turbulence, *Phys. Rev. Lett.* **121**, 124502 (2018).
- [13] W. Hwang and J. Eaton, Creating homogeneous and isotropic turbulence without a mean flow, *Exp. Fluids* **36**, 444 (2004).
- [14] D. R. Webster, A. Brathwaite, and J. Yen, A novel laboratory apparatus for simulating isotropic oceanic turbulence at low Reynolds number, *Limnol. Oceanogr.: Methods* **2**, 1 (2004).
- [15] A. Ghazi Nezami, M. L. Byron, and B. A. Johnson, Laboratory generation of zero mean flow homogeneous isotropic turbulence: Non-grid approaches, *Flow* **3**, E42 (2023).
- [16] A. Glezer and M. Amitay, Synthetic jets, *Annu. Rev. Fluid Mech.* **34**, 503 (2002).
- [17] A. L. McCutchan and B. A. Johnson, An experimental apparatus for generating homogeneous isotropic turbulence, *Exp. Fluids* **64**, 177 (2023).
- [18] B. A. Johnson and E. A. Cowen, Sediment suspension and bed morphology in a mean shear free turbulent boundary layer, *J. Fluid Mech.* **894**, A8 (2020).
- [19] T. M. Lavertu, Differential diffusion in a turbulent jet, Ph.D. thesis, McGill University Libraries, 2006.
- [20] B. Khorsandi, S. Gaskin, and L. Mydlarski, Effect of background turbulence on an axisymmetric turbulent jet, *J. Fluid Mech.* **736**, 250 (2013).
- [21] S. Delbos, V. Weitbrecht, T. Bleninger, P. P. Grand, E. Chassaing, D. Lincot, O. Kerrec, and G. H. Jirka, Homogeneous turbulence at an electrodeposition surface induced by randomly firing jet arrays, *Exp. Fluids* **46**, 1105 (2009).
- [22] T. B. Oehmke and E. A. Variano, A new particle for measuring mass transfer in turbulence, *Exp. Fluids* **62**, 16 (2021).
- [23] A. Pérez-Alvarado, L. Mydlarski, and S. Gaskin, Effect of the driving algorithm on the turbulence generated by a random jet array, *Exp. Fluids* **57**, 20 (2016).
- [24] G. Bellani and E. A. Variano, Homogeneity and isotropy in a laboratory turbulent flow, *Exp. Fluids* **55**, 1646 (2014).
- [25] D. Carter, A. Petersen, O. Amili, and F. Coletti, Generating and controlling homogeneous air turbulence using random jet arrays, *Exp. Fluids* **57**, 189 (2016).
- [26] R. J. Adrian, Particle-imaging techniques for experimental fluid mechanics, *Annu. Rev. Fluid Mech.* **23**, 261 (1991).
- [27] W. Thielicke and E. Stamhuis, PIVlab—towards user-friendly, affordable and accurate digital particle image velocimetry in matlab, *J. Open Res. Softw.* **2**, 30 (2014).
- [28] E. Cowen, S. Monismith, E. Cowen, and S. Monismith, A hybrid digital particle tracking velocimetry technique, *Exp. Fluids* **22**, 199 (1997).
- [29] J. Westerweel and F. Scarano, Universal outlier detection for PIV data, *Exp. Fluids* **39**, 1096 (2005).
- [30] B. Efron and R. J. Tibshirani, *An Introduction to the Bootstrap*, Monographs on Statistics and Applied Probability Vol. 57 (Chapman & Hall/CRC, 1993), pp. 1–436.
- [31] S. B. Pope, *Turbulent Flows* (Cambridge University Press, 2000).
- [32] L. B. Esteban, J. S. Shrimpton, and B. Ganapathisubramani, Laboratory experiments on the temporal decay of homogeneous anisotropic turbulence, *J. Fluid Mech.* **862**, 99 (2019).

- [33] S. Tan, X. Xu, Y. Qi, and R. Ni, Scalings and decay of homogeneous, nearly isotropic turbulence behind a jet array, *Phys. Rev. Fluids* **8**, 024603 (2023).
- [34] Y.-H. Pao, Structure of turbulent velocity and scalar fields at large wavenumbers, *Phys. Fluids* **8**, 1063 (1965).
- [35] M. W. McCorquodale and R. J. Munro, Experimental study of oscillating-grid turbulence interacting with a solid boundary, *J. Fluid Mech.* **813**, 768 (2017).
- [36] W. K. George, The decay of homogeneous isotropic turbulence, *Phys. Fluids A* **4**, 1492 (1992).
- [37] M.-J. Huang and A. Leonard, Power-law decay of homogeneous turbulence at low Reynolds numbers, *Phys. Fluids* **6**, 3765 (1994).
- [38] P. Valente and J. Vassilicos, Dependence of decaying homogeneous isotropic turbulence on inflow conditions, *Phys. Lett. A* **376**, 510 (2012).
- [39] H. S. Kang, S. Chester, and C. Meneveau, Decaying turbulence in an active-grid-generated flow and comparisons with large-eddy simulation, *J. Fluid Mech.* **480**, 129 (2003).
- [40] A. Thormann and C. Meneveau, Decay of homogeneous, nearly isotropic turbulence behind active fractal grids, *Phys. Fluids* **26**, 025112 (2014).
- [41] S. S. Aleyasin and M. F. Tachie, Statistical properties and structural analysis of three-dimensional twin round jets due to variation in Reynolds number, *Int. J. Heat Fluid Flow* **76**, 215 (2019).
- [42] C. S. Greco, A. Ianiro, T. Astarita, and G. Cardone, On the near field of single and twin circular synthetic air jets, *Int. J. Heat Fluid Flow* **44**, 41 (2013).
- [43] B. L. Smith and G. Swift, A comparison between synthetic jets and continuous jets, *Exp. Fluids* **34**, 467 (2003).
- [44] G. Bellani, M. L. Byron, A. G. Collignon, C. R. Meyer, and E. A. Variano, Shape effects on turbulent modulation by large nearly neutrally buoyant particles, *J. Fluid Mech.* **712**, 41 (2012).